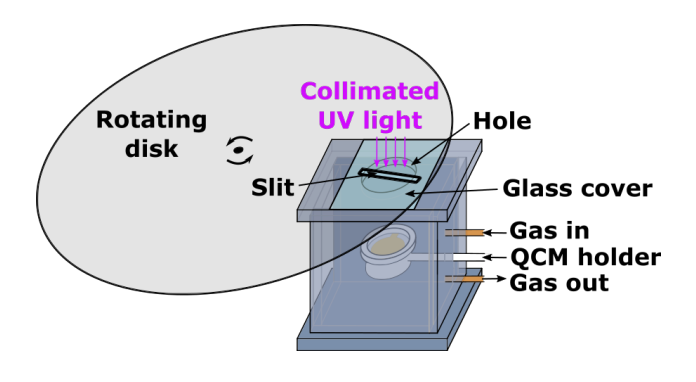
Oxygen Inhibition of Radical Polymerizations Investigated with the Rheometric Quartz Crystal Microbalance

C. Joshua Yeh, Michael Hu, Kenneth R. Shull*

E-mail: k-shull@northwestern.edu

for Table of Contents use only



Abstract

The use of the rheometric quartz crystal microbalance (QCM) as a quantitative cure monitor for photocuring systems was demonstrated. The technique requires the use of films with thicknesses in the micrometer range, and is based on the direct measurement of the rheological properties of the film at a frequency of 15 MHz. To access curing processes much faster than the ~ 1 s resolution of the QCM measurement, a rotating shutter system was designed to capture processes with a temporal resolution of ~ 1 ms. The photocuring process was studied in both air and nitrogen environments, and was applied to a traditional, radically polymerized acrylic system, and a thiol-ene based

system. Thiol-ene systems cured in oxygen reach comparable stiffnesses to those cured in nitrogen, but take longer to cure and contain 1-2.5 wt.% oxygen in the final materials. These results indicate that the QCM can be utilized as an effective photorheometric technique able to provide useful mechanistic insight into photoreactive processes.

Introduction

The facile synthesis of photopolymers allows for the creation of on-demand materials with tunable chemical, mechanical, and structural properties. Recent examples include the development of dental adhesives and resins ^{1–5}, 3D printed structures ^{5,6}, and photopolymerizable and photodegradable hydrogels for biomaterial applications ^{7–10}. Although much of the literature on curing kinetics have been focused on the chemical conversion rate of monomers, there are still many opportunities to investigate the curing kinetics from a rheological perspective. Examination of viscoelasticity during photocuring provides meaningful insight on the local and bulk mechanical and structural properties, which can guide in the strategic engineering of polymeric materials.

A common method to study the photorheology of a polymer system is the parallel plate rheometer that allows light to pass through to the material under testing $^{7,8,11-15}$. This type of setup is suitable for curing polymers that have a starting viscosity of ~ 1 Pa-s (in the monomeric form) and do not exceed ~ 100 MPa in shear modulus. For mechanical testing outside of this range, the sample geometry, applied strain, and/or force transducer need to be adjusted, which can be extremely tedious and can lead to experimental difficulties. Also, other challenges such as oxygen inhibition, inhomogeneous diffusional processes, and thermal rheological complexity can lead to sub-optimal experimental results.

In this study, the utilization of a quartz crystal microbalance (QCM) to study photorheology is described. As suggested by its name, the QCM is traditionally used as a highly sensitive mass balance with a reported areal mass sensitivity in the nanogram range ^{16,17}.

However, from a general perspective, the QCM is more accurately viewed as a shear acoustic reflectometer, capable of simultaneously measuring mass changes and high frequency (MHz) viscoelastic responses of a polymer film in real time.

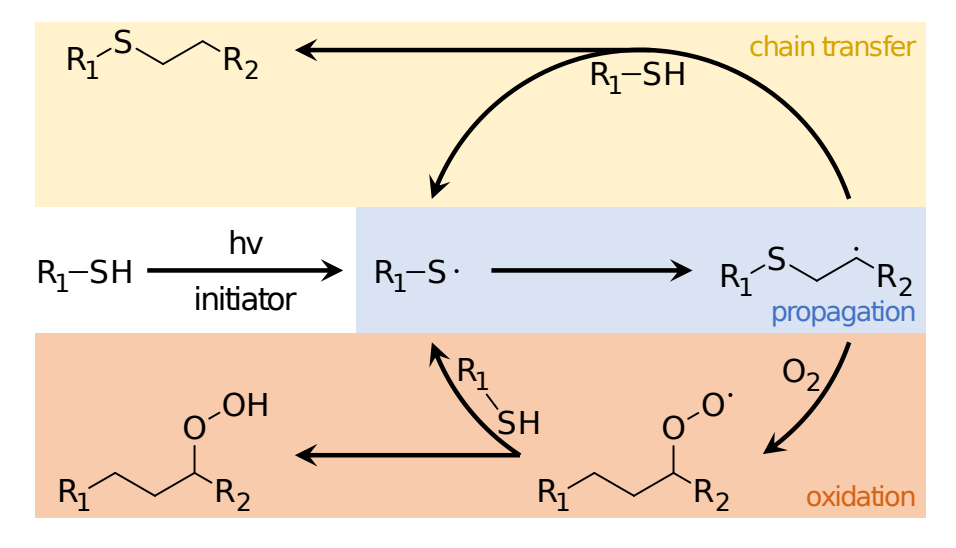
The QCM consists of an AT-cut, single crystal, quartz disk with metal electrodes deposited on both sides of the disk. The quartz disk is connected to an oscillating voltage source which, due to the piezoelectric property of quartz, is used to initiate a mechanical shear wave. The shear wave can be used to probe the high frequency viscoelastic response of a material that is deposited onto one of the electrode surfaces ^{16,18,19}. Because of the low thickness (less than ten microns) of the deposited film and the large exposure area of the top film surface, the entire film is homogeneously cured since diffusional processes through the thickness of the film are fast relative to the experimental time scale. Also, viscoelastic measurements can be performed for an extremely broad property range, including liquid materials with viscosities less than 1 Pa-s and solids with shear moduli greater than 1 GPa ¹⁸. Furthermore, the quartz substrate can be reused multiple times and, if necessary, be replaced economically. The goal of this paper is to demonstrate that the QCM can be employed as a versatile photorheometer, enabling sophisticated experiments that are not possible with traditional rheometers.

Two photopolymers were chosen and investigated: a model acrylate polymer and a thiol-ene polymer undergoing a "click" reaction. The acrylate polymer proceeds with the classical chain growth radical mechanism, whereas the thiol-ene system polymerizes by a step growth radical process²⁰. The effects of varying bursts of direct UV exposure and "dark" periods in between direct irradiation were investigated. Also, due to the reported insensitivity of oxygen inhibition in thiol-enes from reflective IR studies^{20,21}, the impact of oxygen on the viscoelastic curing evolution was examined. Schemes 1 and 2 show the general polymerization and oxidation reactions for the model acrylate and thiol-ene systems, respectively. The peroxy radical formed by the reaction of oxygen with a propagating radical in a traditional vinyl polymer polymerization is no longer reactive towards additional monomer (scheme 1), but in a thiol-ene polymerization the reactive species is regenerated by the abstraction of

a proton from the thiol. While the thiol-ene polymerization is therefore able to proceed in the presence of oxygen, the detailed structure and properties of the resulting polymer are expected to differ from the polymer obtained in the absence of oxygen. One of the aims of this work is to investigate the potential for the quartz crystal microbalance to probe these differences when operating in the rheometric mode that we employ.

$$= \underset{R_1 \text{ initiator}}{\overset{hv}{\underset{R_1 \text{ }}}} \underset{R_2}{\overset{hv}{\underset{R_1 \text{ }}}} \underset{R_2}{\overset{O_2}{\underset{R_1 \text{ }}}} \underset{R_2}{\overset{O_2}{\underset{R_1 \text{ }}}} \underset{R_2}{\overset{O_0}{\underset{R_1 \text{ }}}} \underset{\text{oxygen inhibition}}{\overset{O_2}{\underset{R_1 \text{ }}}} \underset{\text{oxygen inhibition}}{\overset{O_2}{\underset{R_2 \text{ }}}}}$$

Scheme 1: Generalized chain growth radical polymerization and oxygen inhibition reaction for acrylate systems.



Scheme 2: An overview of the thiol-ene polymerization and oxygen scavenging reaction.

Methods and materials

BisGMA sample preparation

The monomer, bisphenol A glycerolate dimethacrylate (bisGMA), was obtained from Sigma-Aldrich (St. Louis, MO) and dissolved in toluene at a 1:1 weight ratio. Approximately 0.5 wt% of 2,2-dimethoxy-2-phenylacetophenone (DMPA) initiator was added to the solution. A UV-visible spectrometry measurement performed on DMPA dissolved in toluene showed that the initiator was excited at wavelengths from 300-370 nm. The chemical structures of bisGMA and DMPA are shown in Figures 1 a and b. The monomer solution was thoroughly mixed, filtered three times with a 0.45 μ m or smaller syringe filter, and protected from ambient light. A \sim 4.5 micron thick film was deposited onto clean QCM crystals using a Laurell, Model WS-650MZ-23NPP, spin coater (North Wales, PA). Prior to spin coating, the QCM crystals were rinsed with ethanol and acetone, blow dried, and exposed to UVozone for 15 min. The film was formed by setting the spin coating speed, acceleration, and spin time to 4500 rpm, 4500 rpm/s, and 75 s, respectively. A Bruker Contour GT optical profilometer (Billerica, MA) was used to determine the optimal spin coating conditions for the preparation of smooth films with the desired film thickness. A film was determined to be "smooth" when the measured characteristic roughness was less than 15% of the film thickness.

Figure 1: Chemical structure of (a) the model acrylate monomer, bisGMA, (b) the photoinitiator, DMPA, (c) the tetra-thiol monomer, PETMP, and (d) the tri-ene monomer, TATATO.

Thiol-ene sample preparation

The monomers, pentaerythritol tetrakis(3-mercaptopropionate) (PETMP) and 1,3,5-triallyl-1,3,5-triazine-2,4,6(1H,3H,5H)-trione (TATATO), were obtained from Sigma Aldrich. The chemical structures of PETMP and TATATO are shown in Figures 1c and d. The two monomers were combined at 0.9:1, 1:1, or 1.1:1 stoichiometric ratios of thiol to ene functional groups. Approximately 0.5 wt% of DMPA initiator was mixed into the PETMP/TATATO monomer mixture. The monomer mixture was stirred for at least 10 min. and subsequently filtered at least twice with a 0.45 μ m or smaller pore size syringe filter. Prior to addition of the initiator, DMPA was dissolved in a small amount of toluene in order to ensure homogeneous dispersion within the monomer mixture; less than 2% of solvent was present in the final monomer mixture. The monomer mixture was protected from ambient light throughout the preparation process. Before spin coating, the QCM crystals were cleaned by rinsing under a stream of ethanol and acetone and exposed to 15 min. of UV-ozone. Spuncast films with thicknesses of $\sim 2.2 \,\mu$ m (9000 rpm, 200 rpm/s, 90 s) or $\sim 3.4 \,\mu$ m (6000 rpm, 200 rpm/s, 90 s) were deposited onto the QCM crystals.

UV curing

Photopolymerization experiments were performed with an Omnicure S1500 UV lamp (Lumen Dynamics, Mississauga, ON, Canada). The UV radiation with a 320-390 nm filter was directed through a liquid filled light guide. A collimator was attached to the end of the light guide in order to produce a uniform one inch diameter spot that covered the entire QCM crystal surface. A custom-built polymethylmethacrylate gas chamber was constructed, as shown in Figure 2a. A hole was placed on the top side of the chamber and covered with a glass slide to allow passage of UV light to the sample. Concerns over the UV absorption of the glass slide was neglected since the irradiation wavelengths is above the absorption range of the glass slide (below $\sim 320 \text{ nm}$)²². The light intensity was measured with a VWR Traceable® light meter (Batavia, IL) at the same surface level as the QCM sample and set to $10 \pm 0.5 \text{ mW/cm}^2$. The interface between the top chamber surface and glass slide was sealed with silicone oil to prevent uncontrolled gas leakage.

A shutter system was used to control the UV exposure burst time. For UV exposure burst times of 0.2 s, the built-in shutter in the Omnicure S1500 UV lamp was used. For burst times less than 0.2 s, a custom shutter system was built. The custom shutter consisted of a rotating disk, constructed from a stiff board, with a predefined slit thickness. The board was wrapped in Al foil in order to prevent residual UV penetration. The UV burst times and intervals times (no UV exposure), graphically represented in Figure 2b, were varied. All curing processes were performed at room temperature.

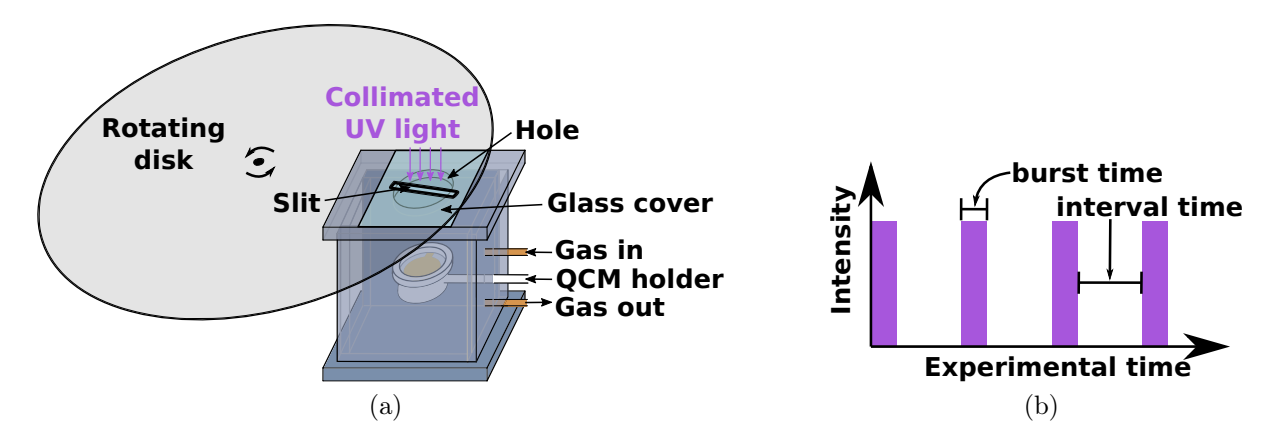


Figure 2: A schematic of (a) the UV curing chamber and (b) a graphical depiction of the burst and interval times on the experimental time axis.

QCM measurements and data acquisition

QCM crystals used in this study consisted of 5 MHz AT-cut quartz disks with gold electrodes deposited on both sides, obtained from Advanced Wave Sensors (Valencia, Spain), Inficon (East Syracuse, NY), and Stanford Research Systems (Sunnyvale, CA) and placed in a Kynar® QCM holder (Inficon). Crystals obtained from these three vendors had the same electrode geometry. Also, control experiments displayed nearly identical quality and response. Prior to use, the crystals were rinsed with ethanol, blow dried, and exposed to 15 minutes of UV/ozone. A vector network analyzer (Makarov Instruments, Thornhill, ON, Canada) supplied an oscillating voltage across a range of frequencies and measured the electrical conductance and susceptance of the QCM crystal. Exciting the quartz crystal at frequencies corresponding odd harmonics of the crystal resonance (5 MHz, 15 MHz, 25 MHz, etc.) produced resonance peaks in the measured electrical admittance. A MATLAB script was used to fit a Lorentz equation 16,23 to the observed peaks so that the resonance frequencies, f_n , and half-bandwidths, Γ_n , were determined, where the subscript, n, denotes the harmonic order (n=1, 3, 5, etc.). Due to the nature of the QCM resonance behavior, anharmonic resonances were observed when $\Gamma_n \gtrsim 10 \, \mathrm{kHz}$, which were accounted for by implementing a multi-peak fitting protocol^{23,24}. To ensure good Lorentz fitting, each scan consisted of at least 300 data points, with the full scan taking no more than half a second to collect.

Measurements were taken at room temperature for each crystal prior to film deposition, in order to obtain reference values for f_n and Γ_n . Films deposited onto the top side of a QCM crystal led to a change in the resonance frequency, Δf_n , and half-bandwidth, $\Delta \Gamma_n$. These changes were used to determine the film properties as described below.

QCM viscoelastic modeling

Several QCM viscoelastic models have been developed ^{18,25–29}. In particular, "Voigt" based models that rely on the spring and dashpot elements are commonly invoked ^{29–32}, despite acknowledgements in its problematic physical interpretation on the frequency dependence of the storage and loss modulus ^{25,33}. Although some "extended" Voigt models incorporate a power law frequency dependence ^{28,31,34}, abidance of the Kramers-Kronig relationship between the storage and loss modulus ³⁵ is unclear.

In the viscoelastic model proposed by Johannsmann ^{25,36}, and the Voinova model ²⁹, a Taylor-expansion series approximation in the film thickness is used to extract the viscoelastic properties, where viscoelasticity can be viewed as a perturbation to the response obtained from a purely inertial mass loading of the film. Accurate determination of the viscoelastic properties requires that thicker films be used:

$$\frac{d}{\lambda} \sim 0.25,\tag{1}$$

where d and λ represent the film thickness and the shear wavelength propagating in the film, respectively. In this case, a more complete numerical method needs to be employed ^{18,37}.

Readers are referred to refs.³⁷ and ¹⁸ for a detailed explanation of the numerical QCM viscoelastic model used in this study. Briefly, three measured values, Δf_{n_1} , Δf_{n_2} , and $\Delta \Gamma_{n_3}$, were used, where n_1 , n_2 , and n_3 represent the harmonic order and $n_1 \neq n_2$. With the assumption that the storage and loss moduli obeys a power law exponent defined by a

constant viscoelastic phase angle, a reasonable assumption within the relatively narrow frequency range considered here, the following three quantities are obtained by solving a series of non-linear equations in MATLAB:

- 1. The mass per unit are of the film, M_A
- 2. The product of the magnitude of the complex shear modulus and film density at the nth harmonic, $|G_n^*| \rho^{-1}$ and
- 3. The viscoelastic phase angle, ϕ_n .

Measurements are recorded for at least two odd harmonics, so that at least four pieces of information were collected: Δf_{n_1} , $\Delta \Gamma_{n_1}$, Δf_{n_2} , and $\Delta \Gamma_{n_2}$. Thus, two separate sets of data could be used to compute M_A , $|G_3^*| \rho$, and ϕ_3 . For example, for data collected at the third and fifth harmonic, two sets of measurements could be used to perform the calculations: $(\Delta f_3, \Delta f_5, \Delta \Gamma_3)$ and $(\Delta f_3, \Delta f_5, \Delta \Gamma_5)$. As a shorthand, these two sets of calculations are herein referred to as "353" and "355", respectively. Ideally, values computed from any combination of datasets yield the same result. However, differences often indicated that systematic errors due to unaccounted anharmonic mode mixing, sample defects, and sample surface roughness were present. As described in previous sections, special care was taken to produce films that were homogeneous, smooth, and free from defects caused by dust particles. For reasons related to experimental repeatability and insensitivity towards edge effects of the crystal 16,25,38,39 , data analysis was focused on the third and fifth harmonics.

To measure properties for an uncured thiol-ene mixture, a clean QCM crystal was immersed in the monomer mixture and protected from light to prevent curing caused by ambient light. This allows the implementation of the semi-infinite QCM viscoelastic relations ¹⁸:

$$|G_n^*| \rho = \left[\frac{-\pi Z_q \Delta f_n}{f_1 \sin(\phi_n/2)}\right]^2 = \left[\frac{\pi Z_q \Delta \Gamma_n}{f_1 \cos(\phi_n/2)}\right]^2 \tag{2}$$

With an estimated film density of $\sim 1\,\mathrm{g/cm^3}$, $|G_3^*|\,\rho$ is effectively a measure of the complex shear modulus magnitude.

and

$$\phi_n = -2 \arctan\left(\frac{\Delta f_n}{\Delta \Gamma_n}\right). \tag{3}$$

The constants, $Z_q = 8.84 \times 10^6 \,\mathrm{kg/\,(m^2 \cdot s)}$ and $f_1 = 5 \,\mathrm{MHz}$, represent the quartz acoustic impedance and fundamental harmonic of the QCM crystal, respectively. This semi-infinite viscoelastic analysis for the uncured thiol-ene mixture is a limiting case of the complete model described by Denolf, et al.³⁷ applicable to low viscosity materials where the decay length of the shear wave is less than the film thickness. In this regime, measurements are no longer sensitive to the film mass, but $|G_n^*| \rho$ and ϕ_n can be obtained from measurements at a single harmonic, using Equations 2 and 3.

Error estimation described in ref.¹⁸ were extended to include correlated random fluctuations (e.g. temperature fluctuations), which were based on statistical analysis of QCM crystal measurements prior to deposition of a viscoelastic film. The applied error methodology can be derived by implementing the matrix formulation of the error propagation law ⁴⁰. Error bars reported herein represent the 95% confidence interval.

Results and discussion

QCM measurements

Representative calculations for "353" and "355" datasets are shown in Figure 3. To check for self consistency and validity of the viscoelastic model, the excluded fourth piece of information in the analysis was back calculated and compared with the experimentally obtained value, as listed in Table 1. The average percent difference between the experimental and predicted values for $\Delta\Gamma_3$ or $\Delta\Gamma_5$ were approximately 6%, which was evidence of good agreement between the "353" and "355" calculations. For all results presented, the "353" and "355" calculations were in good agreement. Thus, quantitative results presented herein can be taken with high confidence. For purposes of clarity, results for the "353" calculations are

plotted, unless indicated.

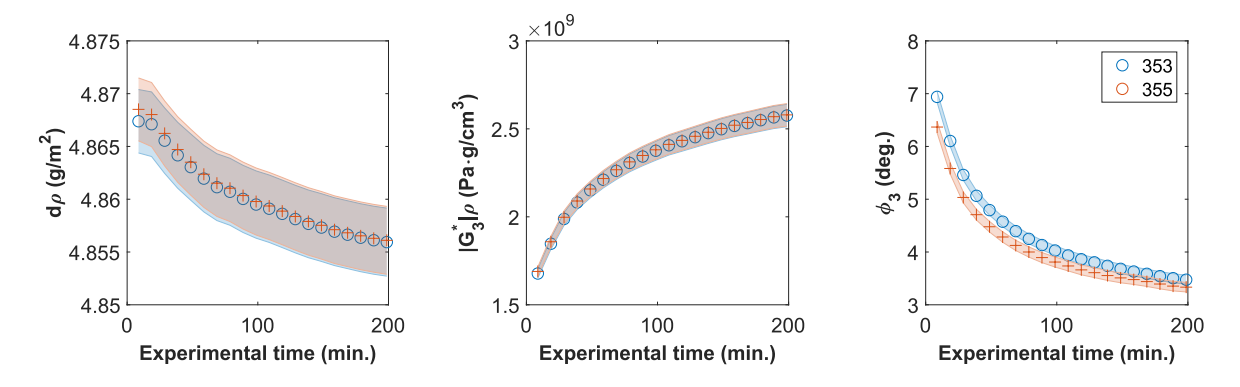


Figure 3: Numerically determined M_A , $|G_3^*| \rho$, and ϕ_3 values for a photopolymerizing bisGMA film. The film was exposed to 0.01 s bursts of UV radiation with 5 s intervals between each burst. Error bars are represented by the sizes of the shaded regions. For clarity, markers are plotted every 10 min.

Table 1: Average percent difference between predicted and measured $\Delta\Gamma_3$ and $\Delta\Gamma_5$ values.

calculation	information used	information not used	* average % difference
type	in analysis	in analysis	in $\Delta\Gamma_3$ or $\Delta\Gamma_5$
353	$\Delta f_3, \Delta f_5, \Delta \Gamma_3$	$\Delta\Gamma_5$	6.4
355	$\Delta f_3, \Delta f_5, \Delta \Gamma_5$	$\Delta\Gamma_3$	-6.1

^{*} in reference to measured values

BisGMA polymer

Due to its prevalence in photopolymer studies $^{1,41-45}$ and simplicity as a single-type monomer reaction that proceeds by chain growth radical polymerization, bisGMA is an ideal model system for this study. The computed values of $|G_3^*| \rho$ and ϕ_3 for this system are shown in Figures 4 and 5. Results shown in Figure 4 are plotted as a function of cumulative UV time scale, representing the total exposure from direct UV radiation. Note that the experimental time differs greatly from the cumulative UV time, since the experimental time depends on both the interval and burst times. For convenience, curing "rates" described in this study are in reference to the cumulative UV exposure time. Concerns over the effects of residual solvents after the spin coating process were determined to be negligible, since the calculated decrease in M_A due to solvent evaporation for all bisGMA datasets was less than 0.5%.

For curing in the presence of oxygen, the viscoelastic properties remained constant throughout the experiment, an expected result since oxygen is a well known inhibitor for chain growth radical polymerization ^{22,46}. Also, the unchanging mechanical properties of the aircured bisGMA dataset provided further justification that effects of residual solvents within the film had a negligible impact on the viscoelastic properties of the film during curing. Under nitrogen curing, changes in both $|G_3^*| \rho$ and ϕ_3 were observed. Extending the interval time or reducing the burst time resulted in an increased curing rate. The results are plotted together on a modified van Gurp-Palmen plot $(\phi_3 \text{ vs. } |G_3^*|\rho)^{47}$ in Figure 5 and collapses onto a linear trend when $|G_3^*| \rho$ is plotted on a logarithmic scale. Changing the interval or burst times shifts the datasets along the master curve. Specifically, efficient curing rates on the cumulative UV time scale (longer interval times and/or shorter burst times) led to a downward shift (higher $|G_3^*| \rho$ and lower ϕ_3) along the master curve. This is a reflection of the structural homogeneity and similarity of the bisGMA samples during photocuring. By extrapolating a linear fit, $\phi_3 = a \times \log_{10}(|G_3^*|\rho) + b$ to $\phi_3 = 0$, where a and b are empirical fitting constants, an estimated upper glassy limit $|G_3^*| \rho = 10^{-b/a}$ of $\sim 3.6\,\mathrm{GPa\cdot g/cm^3}$ can be determined.

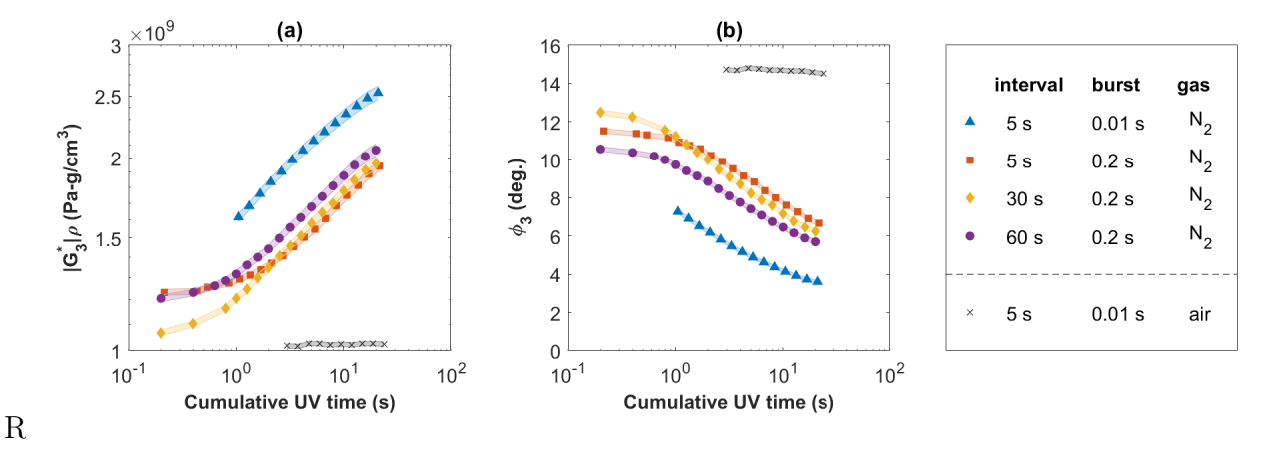


Figure 4: Change in (a) $|G_3^*| \rho$ and (b) ϕ_3 during photocuring of bisGMA as a function of cumulative UV time. Errorbars are drawn as color-corresponding transparent shaded regions. For clarity, markers are displayed in time increments of 0.1 base 10 log units.

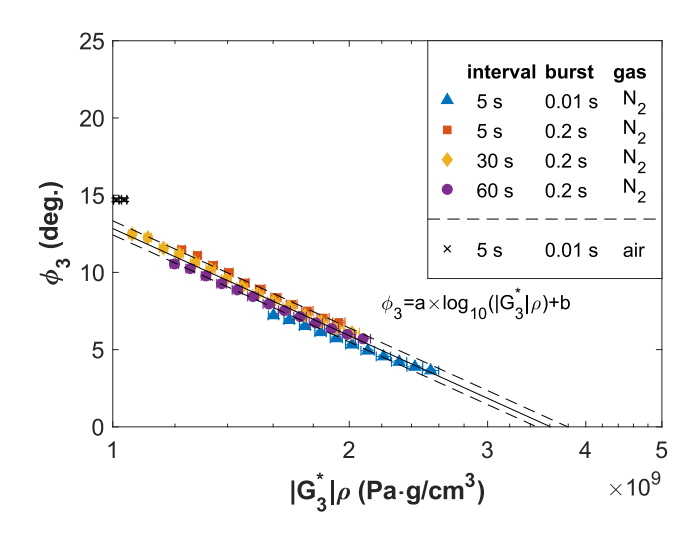


Figure 5: Calculated viscoelastic data plotted on a van Gurp-Palmen plot. A linear fit on a logarithmic x-axis (—, a=-23.04, b=220.2, $R^2=0.9784$) with 95% confidence bounds (–) is shown. The fit is extrapolated for $\phi_3=0$, to estimate the upper limit value for $|G_3^*| \rho$. For clarity, markers are plotted in x-axis increments of 0.02 base 10 log units.

Thiol-ene polymer

Viscoelastic evolution

The viscoelastic evolution for both nitrogen and air cured thiol-ene samples are shown in Figures 6 and 7. Two distinct sets of data in Figure 6a can be identified. Most of the network formation under nitrogen occured within the first 0.1 s of direct UV exposure. On the contrary, polymerization under the presence of oxygen led to a mechanical structure that evolved slowly, only reaching a quasi-steady state after ~ 10 s of total UV irradiation.

The effects of varying interval times for nitrogen-cured samples were small, but observable. Increasing the intervals from 5 s to 60 s, increased $|G_3^*| \rho$, while ϕ_3 remained unchanged. The impact of burst times were larger; decreasing the burst times from 0.2 s to 0.01 s lowered both $|G_3^*| \rho$ and ϕ_3 . The impact of manipulating interval times for air-cured samples were also relatively small, but distinguishable. Increasing the intervals from 5 s to 60 s resulted in lower $|G_3^*| \rho$ and higher ϕ_3 after 10 s of UV irradiation. Varying the burst times appear to have a negligible effect; differences cannot be confidently distinguished due to overlapping

error bars.

Figure 7 suggests structural similarities for nitrogen cured samples sharing the same burst times, since the datasets collapse into a linear master curve on the van Gurp-Palmen plot. Whereas, decreasing the burst time shifts the dataset to the right of the master curve, indicating a differing crosslinked network. The air-cured samples share similar slopes during the early-mid-stage of the curing process. However, past the mid-stage curing, the slopes begin to deviate, due to differences in the quasi-steady state ϕ_3 . An upper glassy limit of $|G_3^*| \rho \sim 3 \,\text{GPa} \cdot \text{g/cm}^3$ at $\phi_3 = 0$ can be estimated by extrapolating a fitted linear curve on the collapsed datasets.

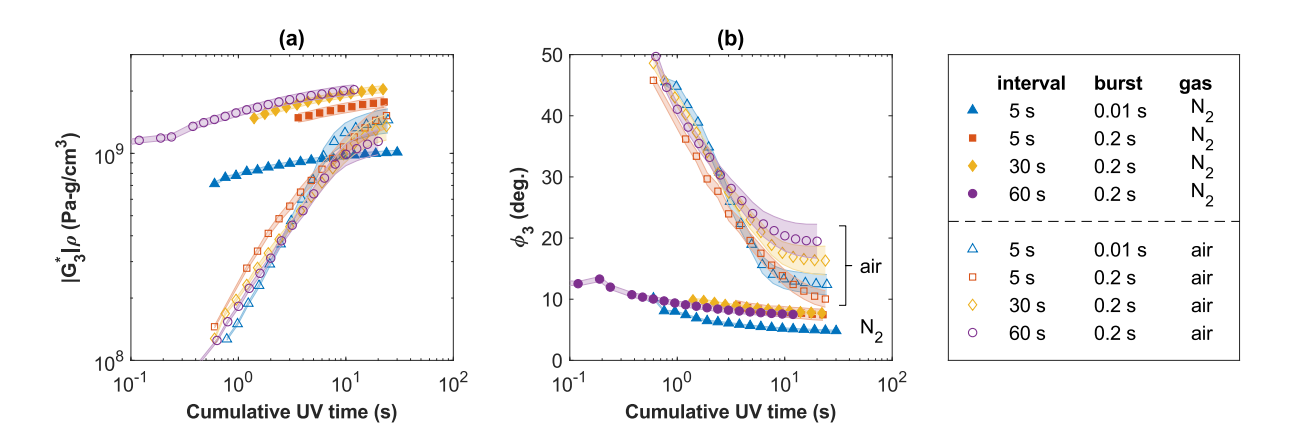


Figure 6: Changes in viscoelastic properties as a function of cumulative UV time. Samples cured in air are represented by open symbols. Samples polymerized in nitrogen are represented by filled markers. For clarity, markers are displayed in time increments of 0.1 base 10 log units. Error bars are drawn as color-corresponding transparent shaded regions.

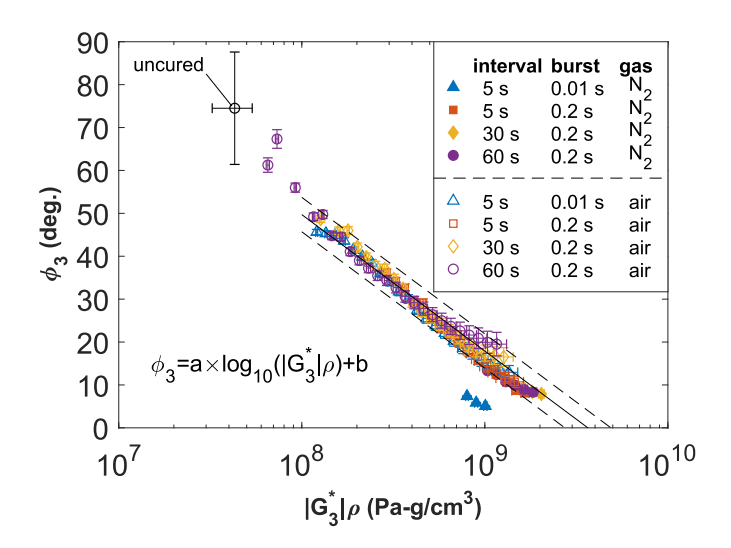


Figure 7: A van Gurp-Palmen plot for the thiol-ene polymer system. Same markers were used as in Figure 6. For clarity, markers are displayed in x-axis increments of 0.05 base 10 log units. The open black circle marker (\bigcirc) represent the uncured thiol-ene monomer mixture, which was determined using the semi-infinite viscoelastic model (see Equations 2 and 3). A linear fit of the collapsed datasets on a logarithmic x-axis (-, a = -31.80, b = 304.1, $R^2 = 0.9426$) with 95% confidence bounds (-) is shown. The fit is extrapolated to $\phi_3 = 0$ as an estimate of the upper limit value for $|G_3^*| \rho$.

Areal mass changes

Changes in M_A during the photopolymerization process are shown in Figure 8, where the calculated percent changes in M_A is in reference to 1 s of UV exposure. The areal mass for the nitrogen cured samples remained relatively constant. However, there are small decreases in areal mass of less than 0.25%, which is attributed to evaporation of residual solvent in the film. Concerns over solvent effects on the interpretation of viscoelastic properties were considered negligible, since there was no clear correlation between changes in M_A and calculated rheological values.

More interestingly, a clear increase in areal mass was observed for samples cured in air. To determine if the mass increase was due to oxygen or water uptake, experiments were repeated under ambient and dry air conditions. Changes in viscoelastic properties and M_A were in agreement within the calculated errors between the two experiments, indicating that oxygen was the primary contributor to the observed areal mass increase shown in Figure 8. From the

standpoint of chemical kinetics, the mechanism by which oxygen is scavenged involves the hydrogen abstraction of a thiol functional group by a peroxide group (formed by a carbon radical and an oxygen molecule)²⁰. This mechanism allows thiol-ene material systems to be insensitive towards oxygen inhibition from a chemical conversion perspective. It is notable that the degree of oxygen incorporation and the effects on the high-frequency rheology of the network can be quantified with the QCM.

We also note that it is difficult to determine the absolute amount of oxygen uptake from the very beginning of the curing process. Changes in the areal mass are quite large within the first half second of total UV exposure, where uncertainties in the Lorentz fitting of the broad resonance peak are relatively large. Empirical extrapolation of the areal mass prior to UV irradiation were considered. However, the fitting is highly dependent on the behavior within the first second of UV exposure, making objective comparisons between datasets difficult. Instead, the areal mass increase in Figure 8 should be interpreted as an estimated lower limit of the oxygen uptake ($\sim 1-2\%$ in M_A after 25 s of UV exposure). Since the oxygen incorporation primarily depends on the number of ene functional groups 20 , an estimate of the upper limit oxygen uptake can be determined ($\sim 16\%$ increase), assuming complete oxidation of the ene functional groups.

Keeping in mind this caveat that quantitative differences in absolute oxygen uptake can be difficult to compare, the rate of oxygen incorporation (when expressed in terms of the cumulative UV exposure time) increases by increasing the interval time or decreasing the burst time. Correlations between the mass and viscoelastic changes cannot be definitively made since the relation between structural details and oxygen incorporation are likely coupled in a complex way. Systematic experiments with thiol and ene monomers of different chemical functionalities, coupled with chemical kinetic simulations, are needed in order to provide further insight on the correlation between oxidative processes and structure formations in these materials.

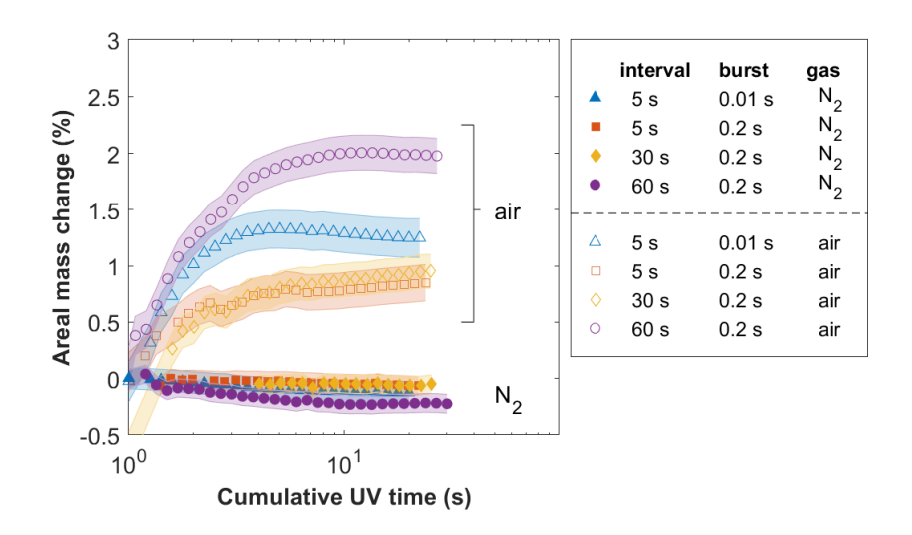


Figure 8: Relative areal mass change after 1 s of cumulative UV exposure. Markers are shown in time increments of 0.05 log units. Error bars are drawn as color-corresponding transparent shaded regions.

Stoichiometric considerations

Stoichiometric effects were considered to assess the sensitivity of the viscoelastic evolution to deviations from a perfect 1:1, thiol to ene mole ratio in these materials. Figure 9 shows the calculated viscoelastic properties for samples cured in air or nitrogen with 5 s interval and 0.01 s burst times. Nitrogen cured samples with a non-1:1, thiol to ene mol ratio displayed a higher $|G_3^*| \rho$ and a slightly higher ϕ_3 . The increase in the complex shear modulus was likely a result of higher chemical conversion and/or degree of crosslinking due to greater availability of unreacted monomers beyond the gel point. Also, a slight increase in viscoelastic phase angle was unsurprising due to unreacted monomers in the film that contribute to a more dissipative behavior. A comparison between samples with a 0.9 or 1.1, thiol to ene mol ratio reveal that excess tri-ene monomers resulted in a higher $|G_3^*| \rho$ and ϕ_3 than excess tetra-thiol monomers. Specifically, a sample with 0.9, thiol to ene mol ratio had approximately 1.3 times more extra monomers than the sample with 1.1, thiol to ene mol ratio, providing a higher potential towards complete conversion and higher ϕ_3 due to higher amounts of freely diffusing monomers.

For films cured in the presence of oxygen, samples with a stoichiometrically imbalanced thiol to ene mol ratio generally had lower $|G_3^*| \rho$ and ϕ_3 , which reflects the structural role of oxygen incorporation into the crosslinking network. The uptake in oxygen, according to the oxygen-scavenging mechanism reported in the literature 20 , should be correlated with the amount of ene monomers in the film. This expectation is consistent with the results shown in Figures 9 and 10. The initial differences in $|G_3^*| \rho$ and ϕ_3 from a 1:1, thiol to ene mol ratio for the sample with excess ene monomers were greater than the film with additional thiol monomers. Also shown in Figure 10, the rate in the change of areal mass after 1 second of UV exposure was highest for the sample with the surplus of ene monomers. In the context of interpreting results from varying burst and interval times, differences in the viscoelastic evolution due to functional group stoichiometry is negligible since observable changes in $|G_3^*| \rho$ and ϕ_3 due to 10% stoichiometric variance is relatively small. Thus, errors of less than 2% for a stoichiometrically balanced thiol to ene mol ratio during sample preparation are unlikely to solely explain the results observed caused by changes in burst and interval times.

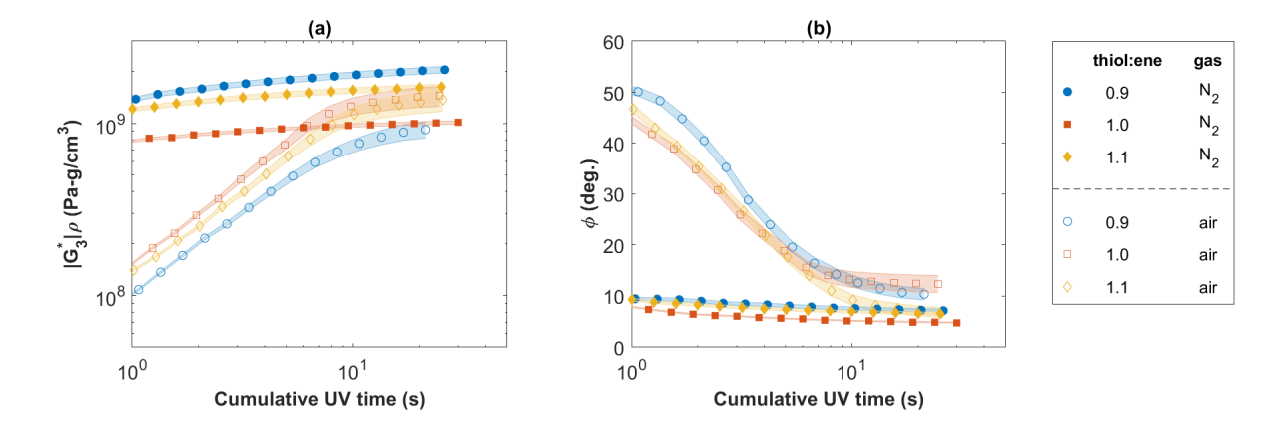


Figure 9: Effects of varying stoichiometric mole ratios of thiol to ene functional groups on the viscoelastic curing evolution for samples cured in air or nitrogen. Datasets shown have the same interval and burst times of 5 s and 0.01 s, respectively. For clarity, markers are displayed in time increments of 0.1 base 10 log units. The size of the error bars are represented by the shaded areas.

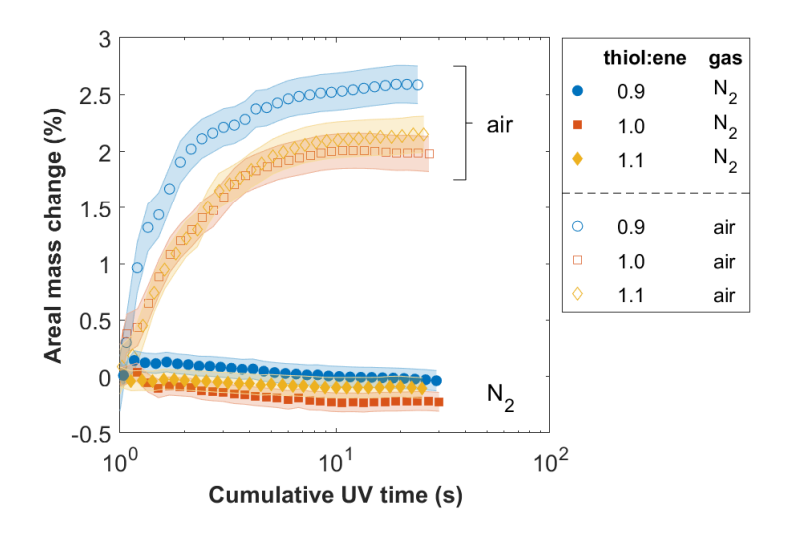


Figure 10: Stoichiometric effects on the relative areal mass changes after 1 s cumulative UV radiation due to oxygen uptake. All samples were exposed to 5 s intervals with 0.01 s bursts of UV light. Markers are shown in time increments of 0.05 log units. The size of the error bars are represented by the shaded areas.

Conclusions

The quartz crystal microbalance was utilized as a high frequency photorheometer capable of monitoring mass and viscoelastic property changes in real time. By implementing the appropriate model of the QCM response ^{18,37}, the effects of changing interval and burst times during UV curing were observed for a model bisGMA material and a thiol-ene system.

Increasing the interval time or decreasing the burst time led to faster viscoelastic curing rates when viewed in terms of the cumulative irradiation time. When plotted in a van Gurp-Palmen form⁴⁷, the bisGMA datasets collapsed onto a master curve, which was fit using a linear equation on a logarithmic modulus axis. The linear fit was extrapolated to $\phi_3 = 0$, giving an upper limit of $\sim 3.6 \,\mathrm{GPa} \cdot \mathrm{g/cm^3}$ for the room-temperature value of $|G_3^*| \,\rho$.

The effects of curing under the presence of oxygen were also explored. Despite the nominal thiol-ene insensitivity towards oxygen inhibition from a chemical kinetics perspective, oxygen incorporation into the network had a clearly observable impact on the viscoelastic curing

evolution. The rate of oxygen uptake was also observable from the calculated mass changes after 1 s of direct UV exposure. When the datasets were plotted in a van Gurp-Palmen form, an upper limit of $\sim 4.0\,\mathrm{GPa} \cdot \mathrm{g/cm^3}$ was obtained for the room-temperature value of $|G_3^*|\,\rho$. Effects of the stoichiometric balance between the thiol and ene functional groups were also explored. Quantitative differences were discerned between samples with excess thiol or ene monomers. Values of $|G_3^*|\,\rho$ and ϕ_3 were higher for the film with excess ene groups compared to the sample with excess thiol groups. For films cured in air, non-stoichiometric, thiol to ene mol ratios generally exhibited lower values of $|G_3^*|\,\rho$ and higher values of ϕ_3 compared to the stoichiometrically balanced thiol to ene ratio. Changes in areal mass showed that the sample with excess ene monomers exhibited a higher rate of oxygen uptake after 1 s of UV irradiation. This result is consistent with the reported mechanism of ene functional groups scavenging molecular oxygen to form peroxides 20 .

Acknowledgments

The authors would like to acknowledge financial support from the 3M Graduate Fellowship Program, the NSF DMR Polymers Program (DMR-1410968, DMR-1710491), and the NSF Graduate Research Fellowship Program (DGE-1324585).

References

- (1) Boulden, J. E.; Cramer, N. B.; Schreck, K. M.; Couch, C. L.; Bracho-Troconis, C.; Stansbury, J. W.; Bowman, C. N. Thiol-ene-methacrylate composites as dental restorative materials. *Dental Materials* 2011, 27, 267–272, DOI: 10.1016/j.dental.2010.11.001.
- (2) Stansbury, J. W. Dimethacrylate network formation and polymer property evolution

- as determined by the selection of monomers and curing conditions. *Dental Materials* **2012**, *28*, 13–22, DOI: 10.1016/j.dental.2011.09.005.
- (3) Sideridou, I. D.; Karabela, M. M. Sorption of water, ethanol or ethanol/water solutions by light-cured dental dimethacrylate resins. *Dental Materials* 2011, 27, 1003–1010, DOI: 10.1016/j.dental.2011.06.007.
- (4) Ferracane, J. L. Resin composite-State of the art. *Dental Materials* **2011**, *27*, 29–38, DOI: 10.1016/j.dental.2010.10.020.
- (5) Stansbury, J. W.; Idacavage, M. J. 3D printing with polymers: Challenges among expanding options and opportunities. *Dental Materials: Official Publication of the Academy of Dental Materials* **2016**, *32*, 54–64, DOI: 10.1016/j.dental.2015.09.018.
- (6) Tumbleston, J. R.; Shirvanyants, D.; Ermoshkin, N.; Janusziewicz, R.; Johnson, A. R.; Kelly, D.; Chen, K.; Pinschmidt, R.; Rolland, J. P.; Ermoshkin, A.; Samulski, E. T.; DeSimone, J. M. Continuous liquid interface production of 3D objects. *Science* 2015, 347, 1349–1352, DOI: 10.1126/science.aaa2397.
- (7) Tibbitt, M. W.; Kloxin, A. M.; Sawicki, L. A.; Anseth, K. S. Mechanical Properties and Degradation of Chain and Step-Polymerized Photodegradable Hydrogels. *Macro-molecules* 2013, 46, 2785–2792, DOI: 10.1021/ma302522x.
- (8) Griffin, D. R.; Kasko, A. M. Photodegradable Macromers and Hydrogels for Live Cell Encapsulation and Release. *Journal of the American Chemical Society* 2012, 134, 13103–13107, DOI: 10.1021/ja305280w.
- (9) Kharkar, P. M.; Kiick, K. L.; Kloxin, A. M. Design of thiol- and light-sensitive degradable hydrogels using Michael-type addition reactions. *Polym. Chem.* **2015**, *6*, 5565–5574, DOI: 10.1039/C5PY00750J.

- (10) Kharkar, P. M.; Kloxin, A. M.; Kiick, K. L. Dually degradable click hydrogels for controlled degradation and protein release. *Journal of Materials Chemistry B* 2014, 2, 5511, DOI: 10.1039/C4TB00496E.
- (11) Schmidt, L. E.; Leterrier, Y.; Vesin, J.-M.; Wilhelm, M.; Månson, J.-A. E. Photorheology of Fast UV-Curing Multifunctional Acrylates. *Macromolecular Materials and Engineering* **2005**, *290*, 1115–1124, DOI: 10.1002/mame.200500229.
- (12) Verney, V.; Commereuc, S. Molecular Evolution of Polymers through Photoageing: A New UV in situ Viscoelastic Technique. *Macromolecular Rapid Communications* 2005, 26, 868–873, DOI: 10.1002/marc.200500073.
- (13) Cook, W. D.; Chausson, S.; Chen, F.; Le Pluart, L.; Bowman, C. N.; Scott, T. F. Photopolymerization kinetics, photorheology and photoplasticity of thiol-ene-allylic sulfide networks. *Polymer International* 2008, 57, 469–478, DOI: 10.1002/pi.2357.
- (14) Khan, S. A.; Plitz, I. M.; Frantz, R. A. In situ technique for monitoring the gelation of UV curable polymers. *Rheologica Acta* **1992**, *31*, 151–160, DOI: 10.1007/BF00373237.
- (15) Chiou, B.-S.; Khan, S. A. Real-Time FTIR and in Situ Rheological Studies on the UV Curing Kinetics of Thiol-ene Polymers. *Macromolecules* 1997, 30, 7322–7328, DOI: 10.1021/ma9708656.
- (16) Johannsmann, D. The Quartz Crystal Microbalance in Soft Matter Research; Soft and Biological Matter; Springer International Publishing: Cham, 2015.
- (17) Caruso, F.; Rodda, E.; Furlong, D. N.; Niikura, K.; Okahata, Y. Quartz Crystal Microbalance Study of DNA Immobilization and Hybridization for Nucleic Acid Sensor Development. Analytical Chemistry 1997, 69, 2043–2049, DOI: 10.1021/ac961220r.
- (18) DeNolf, G. C.; Sturdy, L. F.; Shull, K. R. High-Frequency Rheological Characterization

- of Homogeneous Polymer Films with the Quartz Crystal Microbalance. *Langmuir* **2014**, 30, 9731–9740, DOI: 10.1021/la502090a.
- (19) Sturdy, L.; Casadio, F.; Kokkori, M.; Muir, K.; Shull, K. R. Quartz crystal rheometry: A quantitative technique for studying curing and aging in artists' paints. *Polymer Degradation and Stability* **2014**, DOI: 10.1016/j.polymdegradstab.2014.02.009.
- (20) Hoyle, C. E.; Lee, T. Y.; Roper, T. Thiol-enes: Chemistry of the past with promise for the future. *Journal of Polymer Science Part A: Polymer Chemistry* **2004**, *42*, 5301–5338, DOI: 10.1002/pola.20366.
- (21) Hoyle, C. E.; Bowman, C. N. Thiol-Ene Click Chemistry. *Angewandte Chemie International Edition* **2010**, *49*, 1540–1573, DOI: 10.1002/anie.200903924.
- (22) Odian, G. *Principles of Polymerization*, 4th ed.; John Wiley & Sons: Hoboken, New Jersey, 2004.
- (23) Yoon, S. M.; Cho, N. J.; Kanazawa, K. Analyzing Spur-Distorted Impedance Spectra for the QCM. *Journal of Sensors* **2009**, *2009*, DOI: 10.1155/2009/259746.
- (24) Yeh, C. J. Examination of High Frequency MHz Rheology of Filled Polymer Composites and Photopolymers. Ph.D. thesis, Northwestern University, Evanston, IL, 2017.
- (25) Johannsmann, D. In *Piezoelectric Sensors*; Steinem, C., Janshoff, A., Eds.; Springer Berlin Heidelberg, 2007; Vol. 5; pp 49–109.
- (26) Lucklum, R.; Behling, C.; Hauptmann, P. Role of Mass Accumulation and Viscoelastic Film Properties for the Response of Acoustic-Wave-Based Chemical Sensors. *Analytical Chemistry* 1999, 71, 2488–2496, DOI: 10.1021/ac9812451.
- (27) Martin, E. J.; Mathew, M. T.; Shull, K. R. Viscoelastic Properties of Electrochemically Deposited Protein/Metal Complexes. *Langmuir* 2015, 31, 4008–4017, DOI: 10.1021/acs.langmuir.5b00169.

- (28) Sun, L.; Svedhem, S.; Åkerman, B. Construction and Modeling of Concatemeric DNA Multilayers on a Planar Surface as Monitored by QCM-D and SPR. Langmuir 2014, 30, 8432–8441, DOI: 10.1021/la500716d.
- (29) Voinova, M. V.; Rodahl, M.; Jonson, M.; Kasemo, B. Viscoelastic Acoustic Response of Layered Polymer Films at Fluid-Solid Interfaces: Continuum Mechanics Approach. *Physica Scripta* **1999**, *59*, 391, DOI: 10.1238/Physica.Regular.059a00391.
- (30) Rodahl, M.; Höök, F.; Fredriksson, C.; Keller, C. A.; Krozer, A.; Brzezinski, P.; Voinova, M.; Kasemo, B. Simultaneous frequency and dissipation factor QCM measurements of biomolecular adsorption and cell adhesion. 1997, 107, 229–246, DOI: 10.1039/A703137H.
- (31) Stengel, G.; Höök, F.; Knoll, W. Viscoelastic Modeling of Template-Directed DNA Synthesis. *Analytical Chemistry* **2005**, *77*, 3709–3714, DOI: 10.1021/ac048302x.
- (32) Voinova, M. V.; Jonson, M.; Kasemo, B. 'Missing mass' effect in biosensor's QCM applications. *Biosensors and Bioelectronics* **2002**, *17*, 835–841, DOI: 10.1016/S0956-5663(02)00050-7.
- (33) Reviakine, I.; Johannsmann, D.; Richter, R. P. Hearing What You Cannot See and Visualizing What You Hear: Interpreting Quartz Crystal Microbalance Data from Solvated Interfaces. *Analytical Chemistry* **2011**, *83*, 8838–8848, DOI: 10.1021/ac201778h.
- (34) Liu, Z.; Choi, H.; Gatenholm, P.; Esker, A. R. Quartz Crystal Microbalance with Dissipation Monitoring and Surface Plasmon Resonance Studies of Carboxymethyl Cellulose Adsorption onto Regenerated Cellulose Surfaces. *Langmuir* 2011, 27, 8718–8728, DOI: 10.1021/la200628a.
- (35) Winter, H. H.; Chambon, F. Analysis of Linear Viscoelasticity of a Crosslinking Polymer at the Gel Point. *Journal of Rheology* **1986**, *30*, 367–382, DOI: 10.1122/1.549853.

- (36) Johannsmann, D. Derivation of the shear compliance of thin films on quartz resonators from comparison of the frequency shifts on different harmonics: A perturbation analysis.

 Journal of Applied Physics 2001, 89, 6356.
- (37) DeNolf, G. C.; Haack, L.; Holubka, J.; Straccia, A.; Blohowiak, K.; Broadbent, C.; Shull, K. R. High Frequency Rheometry of Viscoelastic Coatings with the Quartz Crystal Microbalance. *Langmuir* **2011**, *27*, 9873–9879, DOI: 10.1021/la200646h.
- (38) Nunalee, F. N.; Shull, K. R.; Lee, B. P.; Messersmith, P. B. Quartz Crystal Microbalance Studies of Polymer Gels and Solutions in Liquid Environments. *Analytical Chemistry* **2006**, *78*, 1158–1166, DOI: 10.1021/ac0515226.
- (39) Bottom, V. E. *Introduction to Quartz Crystal Unit Design*; Van Nostrand Reinhold Company: New York, 1982.
- (40) Meyer, S. L. Data Analysis for Scientists and Engineers; John Wiley & Sons, Inc.: New York, 1975.
- (41) Cramer, N. B.; Couch, C. L.; Schreck, K. M.; Carioscia, J. A.; Boulden, J. E.; Stansbury, J. W.; Bowman, C. N. Investigation of thiol-ene and thiol-ene-methacrylate based resins as dental restorative materials. *Dental Materials* 2010, 26, 21–28, DOI: 10.1016/j.dental.2009.08.004.
- (42) Cramer, N. B.; Couch, C. L.; Schreck, K. M.; Boulden, J. E.; Wydra, R.; Stansbury, J. W.; Bowman, C. N. Properties of methacrylate-thiol-ene formulations as dental restorative materials. *Dental Materials* 2010, 26, 799-806, DOI: 10.1016/j.dental.2010.04.005.
- (43) Finer, Y.; Santerre, J. P. Salivary Esterase Activity and Its Association with the Biodegradation of Dental Composites. *Journal of Dental Research* 2004, 83, 22–26, DOI: 10.1177/154405910408300105.

- (44) Koin, P. J.; Kilislioglu, A.; Zhou, M.; Drummond, J. L.; Hanley, L. Analysis of the Degradation of a Model Dental Composite. *Journal of Dental Research* 2008, 87, 661– 665, DOI: 10.1177/154405910808700712.
- (45) Finer, Y.; Santerre, J. P. The influence of resin chemistry on a dental composite's biodegradation. *Journal of Biomedical Materials Research Part A* 2004, 69A, 233–246, DOI: 10.1002/jbm.a.30000.
- (46) Drobny, J. Radiation Technology for Polymers, 2nd ed.; CRC Press: Boca Raton, 2010.
- (47) van Gurp,; Palmen, J. Time-Temperature Superposition for Polymeric Blends. *Rheol. Bull.* **1998**, *67*, 5–8.